Linear System Models for Ultrasonic Imaging: Intensity Signal Statistics

Craig K. Abbey, Yang Zhu, Sara Bahramian, and Michael F. Insana, *Fellow, IEEE*

Abstract—Despite a great deal of work characterizing the statistical properties of radio frequency backscattered ultrasound signals, less is known about the statistical properties of demodulated intensity signals. Analysis of intensity is made more difficult by a strong nonlinearity that arises in the process of demodulation. This limits our ability to characterize the spatial resolution and noise properties of B-mode ultrasound images. In this paper, we generalize earlier results on two-point intensity covariance using a multivariate systems approach. We derive the mean and autocovariance function of the intensity signal under Gaussian assumptions on both the object scattering function and acquisition noise, and with the assumption of a locally shift-invariant pulse-echo system function. We investigate the limiting cases of point statistics and a uniform scattering field with a stationary distribution. Results from validation studies using simulation and data from a real system applied to a uniform scattering phantom are presented. In the simulation studies, we find errors less than 10% between the theoretical mean and variance, and sample estimates of these quantities. Prediction of the intensity power spectrum (PS) in the real system exhibits good qualitative agreement (errors less than 3.5 dB for frequencies between 0.1 and 10 cyc/mm, but with somewhat higher error outside this range that may be due to the use of a window in the PS estimation procedure). We also replicate the common finding that the intensity mean is equal to its standard deviation (i.e., signal-to-noise ratio = 1) for fully developed speckle. We show how the derived statistical properties can be used to characterize the quality of an ultrasound linear array for low-contrast patterns using generalized noise-equivalent quanta directly on the intensity signal.

Index Terms—Envelope image, generalized noise-equivalent quanta (GNEQ), image statistics, intensity signal.

I. INTRODUCTION

THE majority of ultrasonic images are viewed as some form of an intensity image. Received pulse-echo signals are demodulated to remove effects of a carrier frequency, and an intensity image is formed that is then used for display, often with subsequent operations of downsampling, scan conversion, interpolation, and amplitude compression. When the object being scanned can be considered as an incoherent scattering medium, the result is an image in which

C. K. Abbey is with the Department of Psychological and Brain Sciences, University of California, Santa Barbara, CA 93106 USA (e-mail: abbey@psych.ucsb.edu).

Y. Zhu, S. Bahramian, and M. F. Insana are with the Departments of Bioengineering and Electronics and Communication Engineering, The Beckman Institute for Advanced Science and Technology, University of Illinois at Urbana-Champaign, IL 61801 USA (e-mail: yangzhu2@illinois.edu; bahrami1@illinois.edu; mfi@illinois.edu).

This paper has supplementary downloadable material available at http://ieeexplore.ieee.org, provided by the authors.

Digital Object Identifier 10.1109/TUFFC.2017.2652451

higher regional intensities in the image correspond to higher regional variability of acoustic impedance in the object. This correspondence of mean image intensity with the variance properties of the object underscores the somewhat more complex statistical relationships in ultrasound images relative to other imaging modalities. Nonetheless, statistical properties are the basis for understanding how images convey information about the object being imaged [1]–[7], and they are a fundamental component of many image-quality measures, including various definitions of signal-to-noise ratio (SNR), contrast-to-noise ratio, cystic resolution, and noise-equivalent quanta (NEQ) [8]–[12].

The physical basis of acoustic backscatter is generally well understood [13]–[17]. Differences in the bulk material properties of mass density and compressibility give rise to mismatched acoustic impedance that causes backscattering of the transmitted pressure pulse as it propagates through tissue. The backscattered waves are coherently detected at the transducer during the receive phase of a pulse-echo sequence. Given that these signals arise from small-scale local variability in tissue, it is natural to model them as a stochastic process. There are many examples of analyzing the statistical properties of backscattered radio frequency (RF) signals to determine structural properties of tissue [18]–[21] or diagnose disease on the basis of spatial texture [22], [23]. However, the nonlinear transform inherent in an intensity signal (or its square root the envelope signal) complicates the propagation of statistical properties through this step. The most common statistical models of intensity or envelope signals are distributions of a single point, which utilize exponential or noncentral chi-squared distributions for the intensity signal and Rayleigh or Rician distributions for the envelope signal [24]–[28]. These distributions are typically justified by making Gaussian assumptions on the underlying RF signal.

While point distributions are useful, many important statistical properties are contained in the spatial correlations between different points in the image domain, which are not captured by point distributions. Smith *et al.* [1] and Wagner *et al.* [2], [3] made important contributions in this area by drawing from the optics and stochastic processes literature [29], [30] to derive two-point covariance functions for intensity and envelope signals. These were also done in the context of sound scattering for fully developed speckle in which Gaussian assumptions are valid. The purpose of this paper is to elaborate the approach of Wagner *et al.* [3] for incoherent scatter in the context of linear systems. We assume fully developed speckle, although not necessarily a uniform scattering medium. We consider the intensity signal for our

derivation, but it has been shown previously [31] that system performance in low contrast detection tasks is relatively stable to amplitude compression and other transformations of the intensity signal.

The linear systems approach [5] allows us to express the mean of the intensity signal as a linear system in which the demodulated pulse intensity acts on the spatial variance map of the object. This allows us to characterize the resolution of the intensity image by the frequency transfer properties of the pulse intensity function. We have also derived the spatial covariance function of the signal function. In the special case of a uniform random scattering field, a locally linear shift-invariant (isoplanetic) system model, and stationary acquisition noise, this allows us to characterize variability of the intensity signal through its power spectrum (PS). Under the assumption of stationary intensity statistics, the intensity-signal transfer function and PS may be combined in a way that is analogous to the concept of generalized NEQ (GNEQ) in X-ray imaging systems [8], [12], [32], [33]. This provides one example of how the derived statistical properties may be used to characterize the quality of the intensity signal.

The derivation in the following pages uses a continuous system model that provides mathematical intuition for the results. Many of the expected values needed for this derivation are technical in nature, and have been placed in the Supplementary Material for this paper in the interest of clarity and space. We show how point statistics (mean and variance) from the derived expressions lead to an SNR of 1, as reported previously [2], [3]. We also provide a brief discussion of the effects of discretization, based on developments in the Supplementary Material. We then describe two validation studies of the expressions for statistical properties of intensity signals. These are comprised of a simulation study in which all the assumptions of the analytic expressions are met, and data from a real system applied to a uniform scattering phantom. The real system shows that these expressions can be applied to predict the intensity statistics of a real device. As a final demonstration of a potential use for the statistical properties derived here, we describe a GNEG comparison of two simulated systems with different pulse bandwidths to show that in addition to improving system resolution, higher bandwidth can lead to improved low-frequency signal quality as well.

II. THEORY

The main theoretical contribution of this paper is the derivation of the mean and autocovariance function of the pulse-echo intensity signal in a linear-systems context. In this section, we describe the mathematical model of image formation and signal processing. In the interest of presenting the results clearly and concisely, we have put most of the technical derivations of the intensity signal statistics into the Supplementary Material associated with this paper. References to sections or equations in the Supplementary Material are preceded by an "S."

A. System Model

RF pulse-echo ultrasonic transducer arrays acquire data as a time signal received over a subaperture and focused through a beamforming operation. These time signals are interleaved across different subaperture positions. For simplicity in the derivations that follow, we will assume that the beam-formed RF data have been scan-converted from a time signal to a 2-D array of spatial position, $g(x, z)$, where x represents the lateral dimension of the plane and z represents the axial dimension. This allows us to represent signal formation for a shift-invariant system as a convolution operation. Let $r_x(t)$ represent the pulse-echo time signal for a subaperture located at position x; then, we define the converted RF data to be $g(x, z) = r_x(2z/c)$, where c is the speed of sound in the medium.

Under the assumption of a locally shift-invariant acquisition, we model signal formation as a noisy 2-D spatial convolution with the underlying object

$$g(x, z) = \int_{-\infty}^{\infty} d\tilde{x}\, d\tilde{z}\, h(x - \tilde{x}, z - \tilde{z}) \gamma(\tilde{x}, \tilde{z}) + \varepsilon(x, z) \quad (1)$$

where $h(x, z)$ is the system function based on backscatter as the pulse propagates through the object of interest, and $\varepsilon(x, z)$ represents acquisition noise. Note that we use the convention of indicating the variables of integration as the differentials immediately following the integration symbol, and so $\int d\tilde{x}\, d\tilde{z}$ indicates a 2-D integral over $\tilde{x}$ and $\tilde{z}$. Zemp et al. [5] have given a detailed description of the physics relating h in (1) to transducer properties, such as the driving voltage of the system, the electromechanical impulse response, and the transmit impulse response. The object scattering function, $\gamma(x, z)$ in (1), represents deviations from the average acoustic impedance of the tissue, which combines the bulk material properties of density and compressibility. In the Fourier domain (the caret symbol, ˆ, is used to indicate a Fourier transform), where u and v represent spatial frequencies corresponding to x and z, the convolution operation in (1) becomes a simple multiplication

$$\hat{g}(u, v) = \hat{h}(u, v)\hat{\gamma}(u, v) + \hat{\varepsilon}(u, v) \quad (2)$$

which is a consequence of the shift-invariance assumption.

B. RF Statistical Properties

We treat both the object and the noise in (1) as samples from zero-mean Gaussian stochastic processes. For the object, a Gaussian process is used to model the impedance variability that leads to incoherent backscatter. The statistical properties of the scattering object are characterized by the autocovariance function (equivalent to the autocorrelation function because of the zero-mean property), which we model as

$$\Sigma_\gamma(x, z, x', z') = \langle \gamma(x, z)\gamma(x', z') \rangle$$
$$= \sigma_{\text{Obj}}^2(x, z)\delta(x - x')\delta(z - z') \quad (3)$$

where the angle brackets indicate a mathematical expectation, and $\sigma_{\text{Obj}}^2(x, z)$ may be thought of as a variance map characterizing the scattering strength of the object. The Dirac delta functions in (3) impose the property that the object reflectivity is essentially uncorrelated at the scales of interest.

The noise process is also characterized by an autocovariance function

$$\Sigma_\varepsilon(x, z, x', z') = \langle \varepsilon(x, z)\varepsilon(x', z') \rangle. \quad (4)$$

It is often the case that we can assume a stationary autocovariance function

$$\Sigma_\varepsilon(\Delta x, \Delta z) = \langle \varepsilon(x, z)\varepsilon(x + \Delta x, z + \Delta z) \rangle. \quad (5)$$

The noise is presumed to be statistically independent of $\gamma(x, z)$. In this situation, we find it useful to characterize the noise in terms of its PS, $S_\varepsilon(u, v)$, which is defined as the Fourier transform of the autocorrelation function. In the Fourier domain

$$\langle \hat{\varepsilon}(u, v)\overline{\hat{\varepsilon}(u', v')} \rangle = S_\varepsilon(u, v)\delta(u - u')\delta(v - v') \quad (6)$$

where the overbar $(-)$ indicates the complex conjugate. For the common choice of bandlimited white noise, the PS is constant within the band limits, $|u| \leq B_x$ and $|v| \leq B_z$, which are often determined indirectly by the sampling rates of the system and associated filters.

The resulting autocovariance function for the RF echo data is given by

$$\begin{aligned}
\Sigma_g(x, z, x', z') &= \langle g(x, z)g(x', z') \rangle \\
&= \int_{-\infty}^{\infty} d\tilde{x}d\tilde{z}h(x - \tilde{x}, z - \tilde{z})h(x' - \tilde{x}, z' - \tilde{z}) \\
&\quad \times \sigma_{\text{Obj}}^2(\tilde{x}, \tilde{z}) + \Sigma_\varepsilon(x, z, x', z')
\end{aligned} \quad (7)$$

where the second expression is obtained from (1), (3), and (4), and the assumption of independence between $\varepsilon(x, z)$ and $\gamma(x, z)$. Note that if the variance map in (3) is constant over x and z, $\sigma_{\text{Obj}}^2(x, z) = \sigma_{\text{Obj}}^2$, then the RF data may be considered a stationary Gaussian process with PS

$$S_g(u, v) = |h(u, v)|^2\sigma_{\text{Obj}}^2 + S_\varepsilon(u, v). \quad (8)$$

This is consistent with previous work [5].

C. Intensity Computation

The making of a B-mode image involves demodulating the RF signal to account for the carrier frequency of the pulse. One common way to implement this is through the formation of a filtered analytic signal by the operation

$$a(x, z) = \int_{-\infty}^{\infty} dudv e^{2\pi i(ux+vz)}\hat{q}(u, v)\hat{g}(u, v) \quad (9)$$

where $\hat{q}(u, v)$ is the demodulation filter. The standard choice is $\hat{q}(u, v) = 2\text{Step}(v)$, where the step function is 0 for negative arguments and 1 for positive arguments. However, we will treat this function generically, since it is possible to implement axial smoothing in the form of an upper limit on the v frequency, or lateral smoothing through an apodizing profile in u. Note that an asymmetric spatial-frequency filter profile results in a complex-valued spatial function. Once the filtered analytic signal has been calculated, the intensity signal is given by the squared magnitude of the analytic signal

$$I(x, z) = a(x, z)\overline{a(x, z)} = |a(x, z)|^2. \quad (10)$$

It should be noted that there may be several additional steps in the creation of a displayed image, such as downsampling, interpolation, and intensity transformations. Our purpose here is to characterize the statistical properties of the intensity signal as computed by (10).

D. Intensity Statistics

Equations (9) and (10) link the intensity signal to the RF data, and hence, deriving statistical properties of intensity signal is a matter of propagating the RF statistics through the demodulation and intensity computations. The demodulation step in (9) is a (complex) linear operation, and so propagation of statistics is well understood even without the complete specification of a probability distribution of the RF signal. However, the intensity computation in (10) is nonlinear, which requires stronger distributional assumptions on the RF for an analytic result, in this case, Gaussian assumptions.

We define two quantities that will be of use in characterizing the statistical properties of the intensity signal. The first we refer to as the analytic system function, defined by applying the demodulation filter to the pulse profile

$$h_a(x, z) = \int_{-\infty}^{\infty} dudv e^{2\pi i(vx+uz)}\hat{q}(u, v)\hat{h}(u, v). \quad (11)$$

Note that in the absence of noise in (1), the analytic system function can be thought of as the kernel of a linear transformation from the object scattering function directly to the analytic signal (see Equation S2). The second quantity of interest we define is the system intensity function, which is given by

$$h_I(x, z) = |h_a(x, z)|^2. \quad (12)$$

Section S1 of the Supplementary Material for this paper shows that the statistical properties of the intensity signal rely on various expectations involving the analytic signal. The two critical expectations for the intensity mean and autocovariance functions are derived there.

1) Mean Intensity: The mean intensity is derived in Equation S12 of the Supplementary Material as

$$\begin{aligned}
\mu_I(x, z) &= \int_{-\infty}^{\infty} d\tilde{x}d\tilde{z}h_I(x - \tilde{x}, z - \tilde{z})\sigma_{\text{Obj}}^2(\tilde{x}, \tilde{z}) \\
&\quad + \int_{-\infty}^{\infty} dudv|\hat{q}(u, v)|^2 S_\varepsilon(u, v).
\end{aligned} \quad (13)$$

This shows that the mean of the intensity signal is a convolution of the variance map with the system intensity function, with an additional nonnegative constant determined by the effect of the demodulation filter magnitude applied to the noise PS. In this context, h_I acts as a point-spread function that maps the spatial variance map of the object to the mean of the intensity signal. The Fourier transform of h_I can be interpreted as the system transfer function from the variance map to the intensity signal.

2) Intensity Covariance: The autocovariance function of the intensity signal is derived in the Supplementary Material as a fourth-order expectation of the analytic signal. It is given

in Equation S15 as

$$\Sigma_I(x, z, x', z')$$

$$= |\int_{-\infty}^{\infty} d\tilde{x} d\tilde{z} h_a(x - \tilde{x}, z - \tilde{z}) h_a(x' - \tilde{x}, z' - \tilde{z}) \sigma_{\text{Obj}}^2(\tilde{x}, \tilde{z})|^2$$

$$+ \left| \int_{-\infty}^{\infty} d\tilde{x} d\tilde{z} h_a(x - \tilde{x}, z - \tilde{z}) \overline{h_a(x' - \tilde{x}, z' - \tilde{z})} \sigma_{\text{Obj}}^2(\tilde{x}, \tilde{z}) \right.$$

$$\left. + \int_{-\infty}^{\infty} du dv e^{2\pi i(u(x-x')+v(z-z'))} |\hat{q}(u, v)|^2 S_\varepsilon(u, v) \right|^2. \tag{14}$$

We will see in Section III below that the first term in this sum, which we refer to as a "coherence term," is often quite small relative to the second and may often be neglected. In this case, we can eliminate the term to get

$$\Sigma_I(x, z, x', z')$$

$$= \left| \int_{-\infty}^{\infty} d\tilde{x} d\tilde{z} h_a(x - \tilde{x}, z - \tilde{z}) \overline{h_a(x' - \tilde{x}, z' - \tilde{z})} \sigma_{\text{Obj}}^2(\tilde{x}, \tilde{z}) \right.$$

$$\left. + \int_{-\infty}^{\infty} du dv e^{2\pi i(u(x-x')+v(z-z'))} |\hat{q}(u, v)|^2 S_\varepsilon(u, v) \right|^2. \tag{15}$$

Equations (13)–(15), and their discrete analog in the Supplementary Material (Equations S25–S27, and S35–S37), represent the main theoretical results of this paper. They show how the echo intensity mean and autocovariance function are directly related to the analytic system function, the object variance map, and the acquisition noise PS under relatively common Gaussian assumptions for fully developed speckle and an isoplanetic imaging system over the region of interest (ROI). In these expressions, the system is assumed to be shift invariant, but the underlying object scattering function may be nonstationary.

E. Special Cases

Two special cases are useful for considering the derived statistical properties of intensity signals in Section II-D. The first is the case of point statistics, specifically the mean and variance at a point (x, z). The mean intensity at a point is given by (13). The variance, given by (15) with $x' = x$ and $z' = z$, is

$$\Sigma_I(x, z, x, z) = \left| \int_{-\infty}^{\infty} d\tilde{x} d\tilde{z} h_I(\tilde{x} - x, \tilde{z} - z) \sigma_{\text{Obj}}^2(\tilde{x}, \tilde{z}) \right.$$

$$\left. + \int_{-\infty}^{\infty} du dv |\hat{q}(u, v)|^2 S_\varepsilon(u, v) \right|^2 \tag{16}$$

which is seen to be the square of the mean value given in (13). Thus, (13) and (16) reproduce the known result [1] that the pointwise SNR of the intensity signal is unity

$$\frac{\mu_I^2(x, z)}{\Sigma_I(x, z, x, z)} = 1 \tag{17}$$

regardless of the signal and noise properties of the RF signal. When the envelope signal ($V = \sqrt{I}$) is considered, this SNR is 1.91.

The second limiting case we consider involves conditions in which the intensity signal may be considered stationary.

The mean intensity in (13) and covariance function in (15) will generally be nonstationary when there is structure in the variance map. However, if the variance map is stationary (i.e., $\sigma_{\text{Obj}}^2(x, z) = \sigma_{\text{Obj}}^2$ irrespective of x and z), then both the mean and the autocovariance function are stationary. A constant variance map causes the mean intensity in (13) to be constant irrespective of x and z, given by

$$\mu_I = \int_{-\infty}^{\infty} du dv |\hat{q}(u, v)|^2 S_g(u, v) \tag{18}$$

where $S_g(u, v)$ is the PS of the RF signal given in (8). For the autocovariance function, a constant variance map allows the function to be written in terms of two arguments, $\Delta x = x - x'$ and $\Delta z = z - z'$. In this case, it is straightforward to derive the stationary autocovariance function from (15) as

$$\Sigma_I(\Delta x, \Delta z) = \left| \int_{-\infty}^{\infty} du dv e^{2\pi i(u\Delta x + v\Delta z)} |\hat{q}(u, v)|^2 S_g(u, v) \right|^2. \tag{19}$$

Note that this is seen to be the square of the mean value in (18) for $\Delta x = \Delta z = 0$, showing that these expressions also obey the SNR relation in (17). To evaluate the autocovariance function, the inverse Fourier transform of $|\hat{q}(u, v)|^2 S_g(u, v)$ is computed, and then, the squared modulus of this quantity is taken. The Fourier transform of $\Sigma_I(\Delta x, \Delta z)$ may be interpreted as the PS of the intensity signal. This approach is adapted to discretely sampled signals in the Supplementary Material.

F. Discrete Systems

The continuous formulation in Section II-A to Section II-E is useful for understanding how the various components of an imaging system combine with the incoherent scattering profile of the object to determine the statistical properties of the echo intensity signal. There are cases where the various integrals can be solved analytically, and others where only numerical solutions are possible. However, experimental data are acquired through sampling, and in many cases of interest, particularly simulations of the sort we use in Section III, the object will be defined on a spatial grid of sample points as well. The data formation analogs of (1) utilize continuous-to-discrete and discrete-to-discrete linear transformations [6]. A more thorough development of discrete signal statistics is given in the Supplemental Material that accompanies this publication. Because of their use in Section III, a few discrete-to-discrete results from that document are given here.

Instead of the spatial position variables, x and z, we denote a discrete array of sampled RF data as a function of lateral and axial indices, n and m. Brackets are used [ ] to indicate functions of a discrete index. So an array of sampled RF data is $g[n, m]$, where $n = 0, \ldots, N - 1$, and $m = 0, \ldots M - 1$. The lateral spacing of samples is given by Δx, and the axial spacing is given by Δz. We also replace the spatial frequency variables, u and v, by discrete spatial frequency indices, k and l. The discrete analog of the mean intensity function in (13) is given by an array of mean values in Equation S35

of the Supplementary Material as

$$\mu_I[n, m] = (\Delta x \Delta z)^2 \sum_{\tilde{n}=0}^{N-1} \sum_{\tilde{m}=0}^{M-1} h_I[n - \tilde{n}, m - \tilde{m}]\sigma_\gamma^2[\tilde{n}, \tilde{m}]$$

$$+ \frac{1}{NM} \sum_{k=0}^{N-1} \sum_{l=0}^{M-1} |q[k, l]|^2 S_\varepsilon[k, l]. \qquad (20)$$

Note that the pulse intensity function is now viewed as a discrete-to-discrete kernel that acts on a discrete variance map. The constant term is now determined by the discrete PS of the acquisition noise, and the squared modulus of the (discrete) demodulation filter. The discrete analog of intensity-signal autocovariance function in (15) is seen in Equation S36 of the Supplementary Material to be

$$\Sigma_I[n, m, n', m']$$
$$= \left| (\Delta x \Delta z)^2 \sum_{\tilde{n}=0}^{N-1} \sum_{\tilde{m}=0}^{M-1} h_a[n - \tilde{n}, m - \tilde{m}] \right.$$
$$\times \overline{h_a[n' - \tilde{n}, m' - \tilde{m}]}\sigma_\gamma^2[\tilde{n}, \tilde{m}]$$
$$\left. + \frac{1}{NM} \sum_{k=0}^{N-1} \sum_{l=0}^{M-1} |\hat{q}[k, l]|^2 S_\varepsilon[k, l]e^{2\pi i\left(\frac{k(n-n')}{N} + \frac{l(m-m')}{M}\right)} \right|^2.$$
$$(21)$$

Here, the analytic pulse profile and its complex complement are used as a discrete-to-discrete kernel acting on the variance map.

Simplifications of these expressions occur for a uniform scattering field (i.e., $\sigma_\gamma^2[n, m] = $ const.) and when the discrete convolution can be approximated as circulant (i.e., with wrap around). As shown in Equation S40, the constant mean of the intensity signal is a constant given by

$$\mu_I = \frac{1}{NM} \sum_{k=0}^{N-1} \sum_{l=0}^{M-1} |q[k, l]|^2 S_g[k, l] \qquad (22)$$

and the autocovariance function is given by

$$\Sigma_I[\Delta n, \Delta m]$$
$$= \left| \frac{1}{NM} \sum_{k=0}^{N-1} \sum_{l=0}^{M-1} |\hat{q}[k, l]|^2 S_g[k, l]e^{2\pi i\left(\frac{k\Delta n}{N} + \frac{l\Delta m}{M}\right)} \right|^2 \qquad (23)$$

as seen in Equation S41, where $S_g[k, l]$ is the discrete PS of the RF data (see Equation S39).

III. VALIDATION STUDIES

We present two validation studies of the statistical properties derived in Section II, a simulation study and a study performed on a physical phantom with a real system. The Monte Carlo simulations test our findings under the assumptions of a scattering medium generated by a Gaussian random process. The purpose of the simulation study is to verify that: 1) the mean and autocovariance functions in (20) and (21) accurately predict sample estimates of the quantities and 2) the coherence term in (14) (or S36) is indeed relatively small and may often be neglected. The physical phantom is used to check how well the RF autocovariance function can be used to predict the intensity PS using (23).
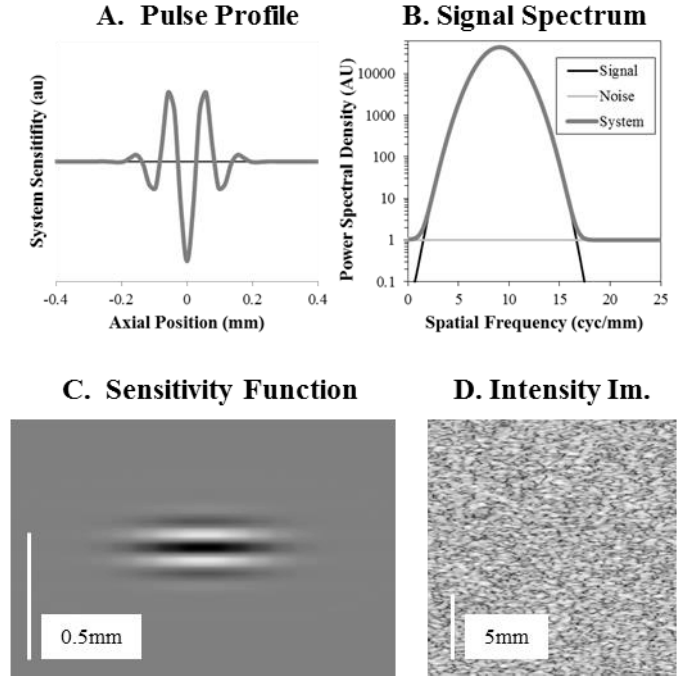

Fig. 1. Simulated system properties. Plots show (A) 7-MHz, 60% bandwidth axial pulse profile and (B) resulting axial signal spectrum at 25-dB eSNR. (C) Displayed sensitivity function shows the lateral component of the pulse. (D) Intensity image shows the speckle pattern arising from a uniform scattering field.

A. Simulated System Model

Various characterizations of this simulated imaging system are shown in Fig. 1. We model a pulse profile that is a Gaussian-modulated sinusoid with a center frequency of 7 MHz and fractional bandwidth [full-width at half-maximum (FWHM)] of 60% across the pulse PS [Fig. 1(A) and (B)]. The axial sampling rate is 40 MSamples/s. We assume white Gaussian acquisition noise with an echo SNR (eSNR) of 30 dB in the focal region at a depth of 4 cm in a scattering medium with fully developed speckle. The lateral pulse profile [Fig. 1(C)] is assumed to be governed by the wavelength, transmit aperture size, and depth of focus.

The resulting system function, $h(x, z)$, is parameterized by an amplitude (A), a Gaussian envelope (with width parameters σ_x and σ_z), and a spatial frequency carrier (f_c) to obtain

$$h(x, z) = -Ae^{-\frac{1}{2}\left(\left(\frac{x}{\sigma_x}\right)^2 + \left(\frac{z}{\sigma_z}\right)^2\right)} \cos(2\pi f_c z). \qquad (24)$$

For a 7-MHz pulse profile and an attenuation-free propagation path at a sound speed of 1540 m/s, the peak spatial frequency is given by 9.09 mm^{-1}. A 60% fractional bandwidth leads to an axial envelope parameter of $\sigma_z = 0.069$ mm in (24). A transmit aperture size of 19.2 mm and 4-cm depth of focus lead to a lateral envelope parameter of $\sigma_x = 0.195$ mm. The axial direction is sampled at an interval of 0.0193 mm (40 MSamples/s), and the lateral direction is sampled at an interval of 0.1 mm. We simulate 192 transmit subaperture windows (N_x) and 1024 axial samples (N_z) for a field of view that is approximately square (19.7 mm in depth and
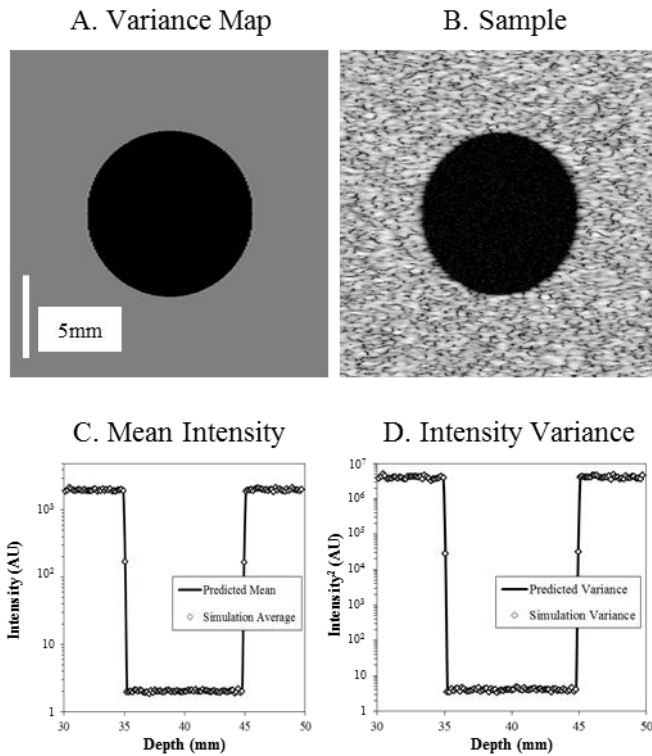
Fig. 2. Comparison of point statistics. (A) Simulation was run with a variance map depicting a 1-cm-diameter hypoechoic lesion. (B) Sample image shows the characteristic speckle pattern of intensity images. The plots compare (C) mean intensity and (D) intensity variance on a vertical line through the center of the hypoechoic region. Simulation statistics were computed from 1000 replications of the simulation procedure, and theoretical predictions were computed using Equations S35 and S37.

19.2 mm wide). An example of the intensity image from a uniform scattering field is shown in Fig. 1(D).

B. Comparison of Statistical Properties in Simulation

As a test of the derived expressions, we compare the mean intensity from Equation S35 [the discrete analog of (13)] to the average intensity computed from 1000 replications of the simulation. In each replication, an independent nonstationary scattering function is sampled from a multivariate Gaussian distribution consistent with the variance map in Fig. 2(A), and an independent realization of acquisition noise is sampled from a Gaussian white noise process. The object variance map contains a clearly visible anechoic "lesion" in the center with a diameter of 1 cm, as seen in Fig. 2(B). The comparison plot shown in Fig. 2(C) suggests very good agreement between the theoretical mean (20) and the empirical average of the intensity signal. The average relative error across the plotted values is 3%.

The variance comparison plot in Fig. 2(D) also shows good agreement between the theoretical variance (21) and the empirical variance measured across the 1000 simulations. In this case, the average relative error is 8%, which reflects lower stability of variance estimation.

An evaluation of the coherent scattering term in Equation S36 [the discrete analog of (14)] finds it generally to
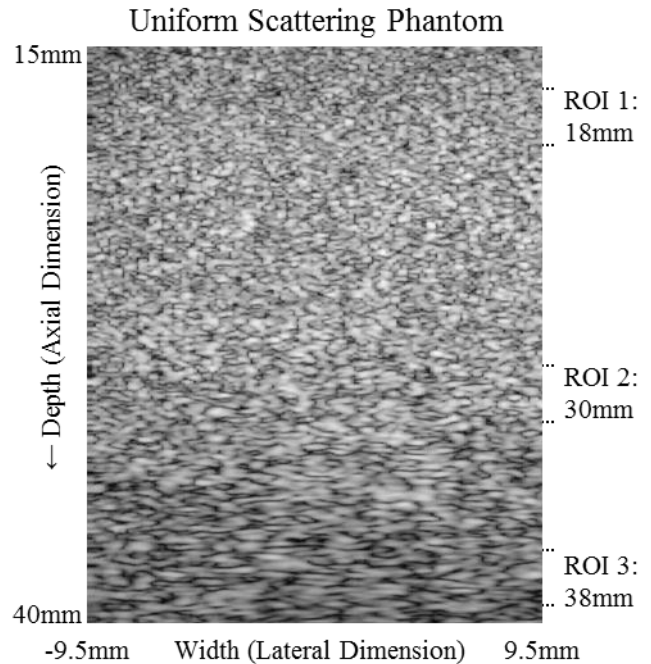

Fig. 3. Uniform scattering phantom. A B-Mode image of the agar scattering phantom is shown with the ROIs for spectral analysis indicated on the left. The image was acquired on an Anteres system linear array with a center frequency of 7.2 MHz. The image has a depth range of 25 mm (15–40 mm) and a width of 19.2 mm. The three ROIs span the lateral dimension, and are centered at 18, 30, and 38 mm in depth. Each ROI consists of 128 samples in the axial dimension and 128 samples in the lateral dimension.

be considerably smaller than the incoherent scattering term, 0.04% on average. However, it achieves a peak contribution of 6.2% relative to the intensity variance at the borders of the lesion. This peak in the coherence term is influenced by the large variation (100%) in the object variance map inside and outside the hypoechoic "lesion." If, instead, the lesion interior is defined by a 50% reduction in scattering variance, the peak relative contribution of the coherence term drops to 0.19%. These relatively small values suggest that neglecting this term will have little effect on analyses at lower contrasts that have less abrupt changes in the variance map.

C. Statistical Properties in a Scattering Phantom

Equations (19) and (23) show that under the assumption of a uniform scattering field (i.e., a constant variance map), the PS of the intensity image is directly related to the PS of the RF data. This provides us an opportunity to check the methodology in a real system using a relatively simple uniform scattering phantom. For this purpose, a gelatin phantom with a uniformly random mixture of cornstarch-particle scatterers was imaged with a Siemens Antares system transmitting 7.2-MHz pulses and sampled at 40 MSamples/s. eSNR in the phantom was approximately 36.4 dB. RF data were collected from the phantom in 66 different locations in order to obtain different (random) arrangements of the scatterers. The data acquisition included 1280 axial samples ranging in depth from 15 mm to almost 40 mm, and 256 lateral samples ranging from −19.2 to 19.2 mm from the center of the transducer. Fig. 3 shows a B-mode image of the scattering phantom.
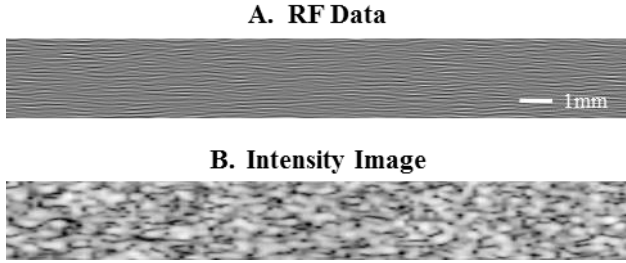
A. RF Data

B. Intensity Image

Fig. 4. Scattering phantom data. (A) RF Data from the 128×128 sample ROI at 30-mm depth is shown as a scan-converted image with the corresponding (B) intensity image shown after logarithmic amplitude compression. The longer horizontal direction of the images is due to the different axial and lateral sampling intervals (0.0193 and 0.15 mm, respectively).
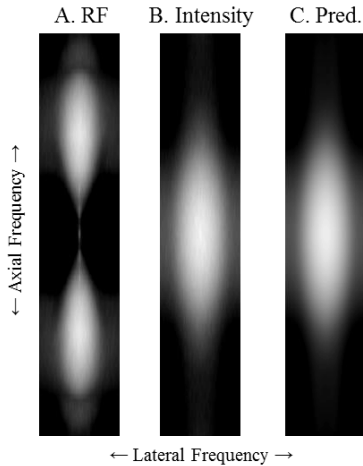

Fig. 5. Power spectra. PS estimates across 66 different locations on the scattering phantom are shown for the scan-converted (A) RF data and (B) intensity images. (C) Predicted PS derived from Equation S39 is also shown. Note that axial frequencies range from -16 to 16 cyc/mm, and lateral frequencies range from -3.3 to 3.3 cyc/mm, resulting in equal frequency increments in the PS images.

A. Axial Intensity Power
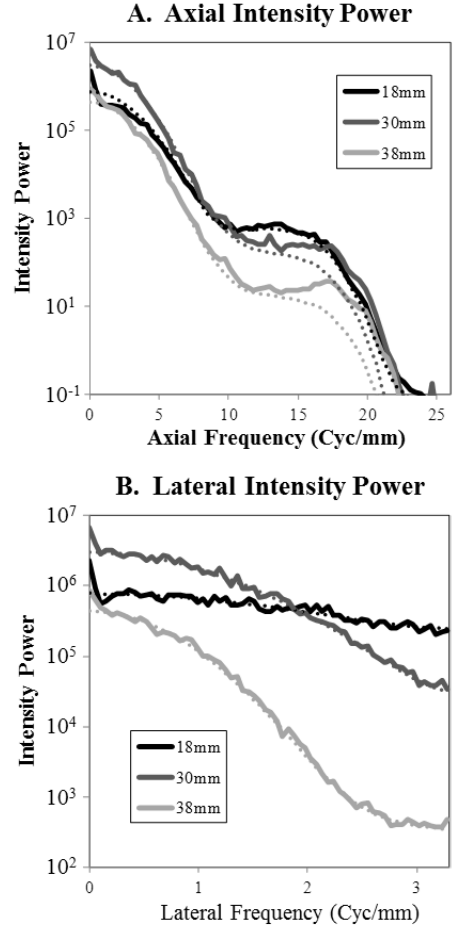

B. Lateral Intensity Power

Fig. 6. Intensity PS plots. Estimated intensity PS plots along (A) axial and (B) lateral dimensions are shown by solid lines color coded for the axial depth of the ROI. The predicted intensity PS is shown for each depth using a dotted line with the same color.

As seen in Fig. 3, the correlation length (i.e., speckle size) changed with depth. To restrict analysis to an area with more uniform statistical properties, a central ROI was used that consisted of 128 axial samples and 128 lateral samples. The axial range of the ROI was 2.5 mm and the lateral range was 19.2 mm, as indicated in Fig. 3. Because of the changing speckle size, we would expect somewhat different results for an ROI taken from a different axial depth.

RF data were converted to an intensity image according to Equations S17 and S18 [the discrete analog of (9) and (10)], using a demodulation filter $[\hat{q}(u, v)]$ that had a value of 2 for axial frequency index values of 1–63 (0.20–12.78 cyc/mm), and zero otherwise. Fig. 4 shows example ROI images for the RF data and the resulting intensity signal, both scan converted into images. Sample estimates of the image PS for the deepest ROI are shown in the RF and intensity domains in Fig. 5(A) and (B). Note that a window function was used in the PS estimates to reduce the effects of spectral leakage [30], since the data were not periodic. A circular window function was used across x and z samples that was constant out to a distance of 32 samples from the center of the ROI, and then, a cosine roll-off was used from distances of 32 samples to 64 samples. The window was zero for samples outside a 64 sample-distance range.

Fig. 5(C) shows the predicted PS using (23), which was used to generate an autocovariance function before computing the Fourier transform. Good qualitative agreement is seen between the intensity PS images [Fig. 5(B) and (C)], which are shown using the same intensity window (10–60 dB). Plots of the measured and predicted intensity power spectra along the axial frequency line are shown in Fig. 6. These suggest good agreement between measurements and theory, with errors less than 3.5 dB for frequencies between 0.1 and 10 cyc/mm. Some larger discrepancies occur at lower frequencies (below 0.1 cyc/mm), where the prediction is higher than PS estimates, and at higher frequencies (above 10 cyc/mm) where the prediction is less than the PS estimate. We believe that the discrepancies are due to the use of the window function in the PS estimate, which was not modeled in (23).

IV. DISCUSSION

Sections II and III show how the model of signal formation for RF data can be used to propagate statistical properties through to the intensity signal under Gaussian assumptions on the reflectivity function. This provides analytic expressions

for the mean and autocovariance function of intensity data. The Supplementary Material shows how these concepts are extended to account for sampling effects. In this section, we discuss some ramifications of these developments.

As described in Section II, the intensity computation (10) involves a nonlinear process that complicates the analysis of statistical properties in the intensity signal. Our theoretical work builds on earlier results by Wagner *et al.* [3] that allows for first and second moments (i.e., mean and autocovariance) of the intensity signal to be calculated. We have extended Wagner's analysis, which focused on two-point statistics, to a linear systems approach where individual points are placed in the context of a system function and acquisition noise.

We find in (13) that the mean intensity signal can be regarded as a convolution of the object variance map with the system intensity function defined in (12), with an additional constant related to the acquisition noise. In this scenario, the system intensity function acts like a point-spread function, and its Fourier Transform, $\hat{h}_I(u, v)$, can be used to characterize the transfer properties of the imaging system for the object variance map. The derived autocovariance functions, given in (14) and (15), are shown to be dependent on the variance map of the object as well as the noise, and hence, the variance properties of the intensity signal will generally be object-dependent. We have shown how this leads to the intensity SNR = 1 relationship in (17).

The object dependence of the autocovariance function makes it difficult to characterize variability in the frequency domain by a PS in a general way, since a nonuniform variance map leads to a nonstationary autocovariance function. However, if we restrict attention to low-contrast effects, which implies a nearly uniform variance map, then we can recover a meaningful PS analysis by taking the Fourier transform of the stationary autocovariance function in (19). We denote this PS as $S_I(u, v)$. If this low-contrast analysis is acceptable, then we may use the statistical properties derived here to characterize the quality of acquired intensity signals.

A. Characterizing Acquisition Through Generalized Noise-Equivalent Quanta

Zemp *et al.* [12] described an approach to characterizing the quality of ultrasound signals through the construct of GNEQ, a quantity defined by Barrett *et al.* [34] and derived from earlier works on photon imaging [8], [35]. The Zemp work defined GNEQ for the RF data, and then showed how this could be used to predict ideal-observer performance for the envelope signal in the limit of low-contrast tasks.

Equations (18) and (19) describe the transfer and noise properties of the intensity signal directly. To evaluate GNEQ of the intensity signal, the Fourier transforms of $h_I(x, z)$ in (12) and $\Sigma_I(\Delta x, \Delta z)$ in (19) are needed. Since $\Sigma_I(\Delta x, \Delta z)$ is the autocovariance function of a stationary random process, its Fourier transform is the PS denoted by $S_I(u, v)$. This allows us to define a GNEQ for the intensity signal as a function of spatial frequency by the ratio

$$\text{GNEQ}_I(u, v) = \frac{|\hat{h}_I(u, v)|^2}{S_I(u, v)} \qquad (25)$$
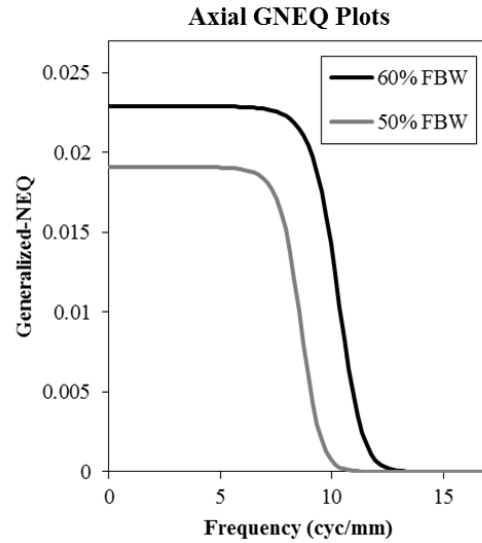

Axial GNEQ Plots

Fig. 7. GNEQ plots for different pulse bandwidths. GNEQ plots of 60% and 50% fractional bandwidth pulses are shown for 7-MHz pulse center frequency on the axial frequency axis.

where the subscript I indicates that the quantity describes the intensity signal.

As an example of GNEQ$_I$ for system comparisons, we revisit the simulation in Section III-A. In addition to the 60% fractional bandwidth system model in (21), we also consider a second system model that has 50% fractional bandwidth (i.e., $\sigma_z = 0.082$ mm), but is, otherwise, identical.

The longer axial pulselength in the 50% bandwidth system leads to a small improvement in eSNR from 30.0 to 30.8 dB. However, Fig. 7 shows that GNEQ$_I$ is uniformly higher for the 60% bandwidth system. At low frequencies, GNEQ$_I$ is 20% greater than the 50% bandwidth system. It also extends to higher spatial frequencies. The half-max axial frequency point of the 60% bandwidth system occurs at 9.47 cyc/mm, compared with 7.96 cyc/mm for the 50% bandwidth system, a 19% improvement in the frequency cutoff and a quantitative measure of how much better the 60% bandwidth system is at visualizing finer scale structures. These results conform to the intuition that higher bandwidth is generally associated with better performance at high resolution. The GNEQ$_I$ plots also adhere to the idea that low-frequency performance may also be improved with a smaller speckle size, as has been noted previously [2]. These performance predictions are a direct consequence of the intensity statistics described earlier.

B. Assumptions and Limitations

Our approach to analyzing intensity statistics has allowed us to derive multivariate statistical properties (i.e., mean and autocovariance) of the intensity signal used to generate B-mode images. Our approach uses a linear systems framework that describes the intensity statistics in terms of a shift-invariant 2-D system function, the acquisition noise PS, and the demodulation filter used to make the analytic signal. However, the approach made use of various assumptions that may limit the applicability of the results.

Most of these assumptions are fairly standard for work of this nature, and have been used previously. The assumption of a Gaussian statistical process that describes the reflectivity function, a locally shift-invariant system model, and independent stationary Gaussian acquisition noise have been used in previous analyses of ultrasound signal statistics [2], [3], [29]. The assumption of cyclic correlations needed to justify the use of finite Fourier transforms on discrete data is also relatively common, and typically justified on the basis that the ROI for analysis is not located near the image boundaries where the assumption is least valid. Extending the current approach to noncirculant correlations for discrete data can be achieved using Toeplitz methods [36], but these will also increase the complexity of the computations. While these assumptions may be common, it is nonetheless important that investigators consider them when applying this approach.

In this paper, we treat the system as a 2-D linear kernel, which neglects aberration, reverberation, and other nonlinear effects of acoustic propagation. In addition, we neglect elevational effects in our system model as well as highly nonstationary components, such as edge waves. Nonlinear effects can be a limiting factor in many applications affecting statistical characterization [37]–[40]. Nonetheless, the characterization of imaging systems in situations where nonlinear effects are not limiting may still be useful. It is our expectation that the techniques derived here can be extended to a fully 3-D nonshift-invariant system model with elevational effects, albeit at the cost of somewhat increased complexity in the formulas describing the mean and autocovariance functions.

V. Conclusion

Under the shift-invariance assumption, our analysis shows how the statistical properties of an ultrasonic intensity image from an incoherent scattering medium depend on the transfer function of the system, acquisition noise, and the demodulation filter used to create the analytic signal. This analysis is made difficult by the strong nonlinearity in the intensity computation. Our approach builds on the work of Smith *et al.* [1] and Wagner *et al.* [3] who use a result from fourth-order Gaussian correlations [30]. Our contribution has been to derive the intensity statistics in the context of a locally shift-invariant linear imaging system [5] that generates the RF data from which an intensity image is computed. This allows us to present general expressions for the multivariate mean and autocovariance of the intensity signal under the Gaussian assumptions (fully developed speckle) used by Wagner *et al.* [3]. We have analyzed special cases of these expressions for point statistics (mean and variance) and a stationary scattering medium (intensity point-spread function and PS).

We have verified the validity of our findings by comparing statistical properties in a simulation and a commercial imaging system. The simulation suggests that the coherence term in the full autocovariance expression may be small enough to be neglected in many circumstances. The experiment with data from the Antares system shows that the RF PS can be used to obtain a relatively accurate prediction of the intensity PS for a uniform incoherent scattering medium.

Our results provide analytic expressions that can be used when statistical properties are needed for evaluating the quality of intensity images. As an example of how this may be accomplished, we use the results to derive an intensity signal analog of the GNEQ, and we show how this can be used to evaluate the effect of axial fractional bandwidth in the system model. The work here has focused on the intensity signal, but previous findings suggest that reasonable compressions of the intensity signal (e.g., envelope or log-envelope) should have relatively little effect on the performance of the imaging system [31].

References

[1] S. W. Smith, R. F. Wagner, J. M. Sandrik, and H. Lopez, "Low contrast detectability and contrast/detail analysis in medical ultrasound," *IEEE Trans. Sonics Ultrason.*, vol. SU-30, no. 3, pp. 164–173, May 1983.

[2] R. F. Wagner, S. W. Smith, J. M. Sandrik, and H. Lopez, "Statistics of speckle in ultrasound B-scans," *IEEE Trans. Sonics Ultrason.*, vol. SU-30, no. 3, pp. 156–163, May 1983.

[3] R. F. Wagner, M. F. Insana, and D. G. Brown, "Statistical properties of radio-frequency and envelope-detected signals with applications to medical ultrasound," *J. Opt. Soc. Amer. A*, vol. 4, pp. 910–922, May 1987.

[4] H. H. Barrett, "Objective assessment of image quality: Effects of quantum noise and object variability," *J. Opt. Soc. Amer. A*, vol. 7, pp. 1266–1278, Jul. 1990.

[5] R. J. Zemp, C. K. Abbey, and M. F. Insana, "Linear system models for ultrasonic imaging: Application to signal statistics," *IEEE Trans. Ultrason., Ferroelect., Freq. Control*, vol. 50, no. 6, pp. 642–654, Jun. 2003.

[6] H. H. Barrett and K. J. Myers, *Foundations of Image Science*. Hoboken, NJ, USA: Wiley, 2004.

[7] C. K. Abbey, N. Q. Nguyen, and M. F. Insana, "Effects of frequency and bandwidth on diagnostic information transfer in ultrasonic B-mode imaging," *IEEE Trans. Ultrason., Ferroelect., Freq. Control*, vol. 59, no. 6, pp. 1115–1126, Jun. 2012.

[8] R. F. Wagner and D. G. Brown, "Unified SNR analysis of medical imaging systems," *Phys. Med. Biol.*, vol. 30, no. 6, pp. 489–518, 1985.

[9] J. M. Thijssen, G. Weijers, and C. L. de Korte, "Objective performance testing and quality assurance of medical ultrasound equipment," *Ultrasound Med. Biol.*, vol. 33, pp. 460–471, Mar. 2007.

[10] D. A. Guenther and W. F. Walker, "Generalized cystic resolution: A metric for assessing the fundamental limits on beamformer performance," *IEEE Trans. Ultrason., Ferroelect., Freq. Control*, vol. 56, no. 1, pp. 77–90, Jan. 2009.

[11] N. Q. Nguyen, C. K. Abbey, and M. F. Insana, "Objective assessment of sonographic: Quality II acquisition information spectrum," *IEEE Trans. Med. Imag.*, vol. 32, no. 4, pp. 691–698, Apr. 2013.

[12] R. J. Zemp, M. D. Parry, C. K. Abbey, and M. F. Insana, "Detection performance theory for ultrasound imaging systems," *IEEE Trans. Med. Imag.*, vol. 24, no. 3, pp. 300–310, Mar. 2005.

[13] J. Gore and S. Leeman, "Ultrasonic backscattering from human tissue: A realistic model," *Phys. Med. Biol.*, vol. 22, no. 2, p. 317, 1977.

[14] M. Fatemi and A. C. Kak, "Ultrasonic B-scan imaging: Theory of image formation and a technique for restoration," *Ultrason. Imag.*, vol. 2, no. 1, pp. 1–47, 1980.

[15] J. A. Jensen and N. B. Svendsen, "Calculation of pressure fields from arbitrarily shaped, apodized, and excited ultrasound transducers," *IEEE Trans. Ultrason., Ferroelect., Freq. Control*, vol. 39, no. 2, pp. 262–267, Mar. 1992.

[16] K. K. Shung and G. A. Thieme, *Ultrasonic Scattering in Biological Tissues*. Boca Raton, MA, USA: CRC Press, 1993.

[17] B. A. J. Angelsen, *Ultrasound Imaging: Waves, Signals and Signal Processing*, vol. I & II. Norway, MA USA: Emantec, 2000.

[18] F. G. Sommer, R. T. Hoppe, L. Fellingham, B. A. Carroll, H. Solomon, and S. Yousem, "Spleen structure in Hodgkin disease: Ultrasonic characterization. Work in progress," *Radiology*, vol. 153, pp. 219–222, Oct. 1984.

[19] M. F. Insana, R. F. Wagner, D. G. Brown, and T. J. Hall, "Describing small-scale structure in random media using pulse-echo ultrasound," *J. Acoust. Soc. Amer.*, vol. 87, pp. 179–192, Jan. 1990.

[20] M. L. Oelze, W. D. O'Brien, Jr., J. P. Blue, and J. F. Zachary, "Differentiation and characterization of rat mammary fibroadenomas and 4T1 mouse carcinomas using quantitative ultrasound imaging," *IEEE Trans. Med. Imag.*, vol. 23, no. 6, pp. 764–771, Jun. 2004.

[21] F. L. Lizzi, S. K. Alam, S. Mikaelian, P. Lee, and E. J. Feleppa, "On the statistics of ultrasonic spectral parameters," *Ultrasound Med. Biol.*, vol. 32, pp. 1671–1685, Nov. 2006.

[22] P. M. Shankar, V. A. Dumane, C. W. Piccoli, J. M. Reid, F. Forsberg, and B. B. Goldberg, "Computer-aided classification of breast masses in ultrasonic B-scans using a multiparameter approach," *IEEE Trans. Ultrason., Ferroelect., Freq. Control*, vol. 50, no. 8, pp. 1002–1009, Aug. 2003.

[23] P. M. Shankar *et al.*, "Classification of breast masses in ultrasonic B scans using Nakagami and K distributions," *Phys. Med. Biol.*, vol. 48, pp. 2229–2240, Jul. 2003.

[24] D. Middleton, *An Introduction to Statistical Communication Theory.* New York, NY, USA: McGraw-Hill, 1960.

[25] D. Middleton, "Some general results in the theory of noise through non-linear devices," *Quart. Appl. Math.*, vol. 5, no. 4, pp. 445–498, 1948.

[26] S. O. Rice, "Mathematical analysis of random noise," *Bell Syst. Tech. J.*, vol. 23, no. 3, pp. 282–332, 1944.

[27] S. O. Rice, "Mathematical analysis of random noise," *Bell Syst. Tech. J.*, vol. 24, no. 1, pp. 146–158, 1945.

[28] D. O. North, "An analysis of the factors which determine signal/noise discrimination in pulsed-carrier systems," *Proc. IEEE*, vol. 51, no. 8, pp. 1016–1027, 1963.

[29] J. W. Goodman, *Statistical Optics.* New York, NY, USA: Wiley, 1985.

[30] J. S. Bendat and A. G. Piersol, *Random Data: Analysis and Measurement Procedures.* New York, NY, USA: Wiley, 1971.

[31] J. M. Thijssen, B. J. Oosterveld, and R. F. Wagner, "Gray level transforms and lesion detectability in echographic images," *Ultrason. Imag.*, vol. 10, no. 3, pp. 171–195, 1988.

[32] J. C. Dainty and R. Shaw, *Image Science: Principles, Analysis and Evaluation of Photographic-Type Imaging Processes.* New York, NY, USA: Academic, 1974.

[33] C. E. Metz, R. F. Wagner, K. Doi, D. G. Brown, R. M. Nishikawa, and K. J. Myers, "Toward consensus on quantitative assessment of medical imaging systems," *Med. Phys.*, vol. 22, pp. 1057–1061, Jul. 1995.

[34] H. H. Barrett, J. L. Denny, R. F. Wagner, and K. J. Myers, "Objective assessment of image quality. II. Fisher information, Fourier crosstalk, and figures of merit for task performance," *J. Opt. Soc. Amer. A, Opt. Image Sci.*, vol. 12, pp. 834–852, May 1995.

[35] R. Shaw, "The equivalent quantum efficiency of the photographic process," *J. Photogr. Sci.*, vol. 11, no. 4, pp. 199–204, 1963.

[36] N. Q. Nguyen, C. K. Abbey, and M. F. Insana, "Robustness of Wiener filtering as an approximation to the Bayesian observer stragegy," in *Proc. IEEE Ultrason. Symp. (IUS)*, Oct. 2010, pp. 995–998.

[37] G. E. Trahey and S. W. Smith, "Properties of acoustical speckle in the presence of phase aberration. Part I: First order statistics," *Ultrason. Imag.*, vol. 10, no. 1, pp. 12–28, 1988.

[38] S. W. Smith, G. E. Trahey, S. M. Hubbard, and R. F. Wagner, "Properties of acoustical speckle in the presence of phase aberration. Part II: Correlation lengths," *Ultrason. Imag.*, vol. 10, no. 1, pp. 29–51, 1988.

[39] L. Nock, G. E. Trahey, and S. W. Smith, "Phase aberration correction in medical ultrasound using speckle brightness as a quality factor," *J. Acoust. Soc. Amer.*, vol. 85, pp. 1819–1833, Jun. 1989.

[40] M. E. Anderson, M. S. McKeag, and G. E. Trahey, "The impact of sound speed errors on medical ultrasound imaging," *J. Acoust. Soc. Amer.*, vol. 107, no. 6, pp. 3540–3548, 2000.

Craig K. Abbey received the Ph.D. degree in applied mathematics from the University of Arizona, Tucson, AZ, USA, in 1998.

He was a Post-Doctoral Fellow in medical physics with the Cedars-Sinai Medical Center and University of California at Los Angeles, Los Angeles, CA, USA, from 1998 to 2001. From 2001 to 2004, he was a Member of the Faculty in Biomedical Engineering, University of California at Davis, Los Angeles, CA, USA. His primary affiliation is in the Department of Psychological and Brain Sciences with the University of California at Santa Barbara, Santa Barbara, CA, USA. His current research interests include the transfer of diagnostic information in medical imaging systems utilizing theoretical analysis of image statistics, and visual psychophysics for evaluating human observer performance.

Yang Zhu was born in Zhejiang, China, in 1989. She received the B.S. degree in electrical engineering from Purdue University, West Lafayette, IN, USA, in 2012, and the M.S. degree in electrical engineering from the University of Michigan, Ann-Arbor, MI, USA, in 2014. She is currently pursuing the Ph.D. degree with the Bioengineering Department, University of Illinois at Urbana-Champaign, Champaign, IL, USA.

Her current research interests include acoustic imaging, biomedical signal processing, and cancer diagnosis.

Sara Bahramian is currently pursuing the Ph.D. degree with the Electrical and Computer Engineering Department, the University of Illinois at Urbana-Champaign, Champaign, IL, USA.

Her current research interests include the intersection of image science and signal/image processing. In her Ph.D. research, she studies the transfer of diagnostic information in ultrasonic imaging process for the purpose of improving the ultrasound image display. The application of her research in the detection of breast microcalcifications have been patented, in 2014.

Ms. Bahramian has been a recipient of Computational Science and Engineering Fellowship at the University of Illinois at Urbana–Champaign, in 2013 and 2014.

Michael F. Insana (M'85–SM'06–F'12) received the Ph.D. degree in medical physics from the University of Wisconsin - Madison, Madison, WI, USA, in 1983.

He is currently a Willett Professor of Engineering and a Faculty Member with the Department of Bioengineering and Department of Electronics & Communication Engineering, the University of Illinois at Urbana–Champaign, Champaign, IL, USA. He also leads the Bioimaging Science and Technology Group with the Beckman Institute for Advanced Science and Technology, Urbana, IL, USA. He was the Head of the Department of Bioengineering in its early years from 2008 to 2013. His current research interests include medical ultrasonic imaging as applied to cancer diagnosis and treatment monitoring. He develops instrumentation and methods for imaging soft tissue microstructure, viscoelasticity, and blood flow, and task-based optimization methods for designing and evaluating sonographic systems. He has also developed novel methods for characterizing large-scale network and other nonlinear systems.

Dr. Insana is a Fellow of the Acoustical Society of America, Institute of Physics, and American Institute of Medical and Biological Engineering. He is currently Editor-in-Chief of IEEE TRANSACTIONS ON MEDICAL IMAGING, and Co-Chair of the 2016 and 2018 Gordon Conferences on Image Science.